Electronic Supplementary Information (ESI)

for

Multifunctional Nanocomposite for Luminescence Resonance Energy Transfer-Guided Synergistic Monitoring and Therapy under Single Near Infrared Light

Yu Zhang,[a] Ting-Ting Shen,[a] Hao-Li Zhang,[a] Alexander M. Kirillov,[b] Hui-Juan Cai,[a] Jiang Wu,[a] Wei-Sheng Liu,[a] and Yu Tang[*a]

Table of Contents

[a.] State Key Laboratory of Applied Organic Chemistry, Key Laboratory of Nonferrous Metal Chemistry and Resources Utilization of Gansu Province, College of Chemistry and Chemical Engineering, Lanzhou University, Lanzhou 730000 (China)

E-mail: tangyu@lzu.edu.cn

[b.] Centro de Quimica Estrutural, Complexo I, Instituto Superior Tecnico, Universidade de Lisboa, Av. Rovisco Pais, Lisbon 1049-001 (Portugal)

S1. Experimental Section

S1.1 Materials

Europium nitrate (Eu(NO$_3$)$_3$·6H$_2$O) was prepared by reacting Eu$_2$O$_3$ (99.99%, Shanghai Yuelong) with nitric acid, and then superfluous nitric acid was removed. Tetraethoxysilane (TEOS), phenyltriethoxysilane (PTES), hexadecyltrimethylammonium chloride (CTAC), chloroauric acid (HAuCl$_4$·4H$_2$O), 3-(trimethoxysilyl)propyl methacrylate (MPS), N-isopropylacrylamide (NIPAM), methacrylic acid (MAA), diphenyl(2,4,6-trimethylbenzoyl)phosphine oxide (TPO), sodium borohydride (NaBH$_4$), sodium iodide (NaI), L-ascorbic acid (AA), carbazole, 1-bromopentane, acetylchloride, ethyl trifluoroacetate, 1-ethyl-3-[3-dimethylaminopropyl]carbodiimide hydrochloride (EDC), N-hydroxysuccinimide (NHS), and anhydrous dimethyl sulfoxide (DMSO) were purchased from J&K Scientific Ltd. cRGD (cyclic(Arg-Gly-Asp-D-Phe-Lys)) was obtained from GL Biochem Ltd. Doxorubicin hydrochloride (DOX) was obtained from Beijing Huafeng United Technology Co., Ltd. (Beijing, China). 1,10-Phenanthroline (phen) was purchased from Alfa Aesar. The reagents were all of analytical reagent (AR) grade. 3-(4,5-Dimethylthiazol-2-yl)-2,5-diphenyltetrazolium bromide (MTT) and 4% paraformaldehyde were purchased from Solarbio Co. Ltd. Dulbecco's Modified Essential Medium (DMEM), Ham's F12 (F12), fetal bovine serum (FBS), and trypsin-EDTA solution were purchased from Gibco.

S1.2. Synthesis of the nanocomposite

Synthesis of 4,4,4-trifluoro-1-(9-hexylcarbazole-3-yl)-1,3-butanedione (HTHA). HTHA was synthesized according to the previous report.[S1] 16.7 g of carbazole (100 mmol) and 6.0 g of NaOH (150 mmol) were dissolved in acetone (100 mL) and refluxed for 2 h. After cooling to room temperature, 14 mL 1-bromopentane (16.5 g, 100 mmol) were added and refluxed for 24 hours. The solvent was removed by rotary evaporation and 200 mL water was added with stirring. The residual solid was filtered and recrystallized from EtOH and water to give 9-hexyl-carbazole. Then AlCl$_3$ (5.2 g, 40 mmol) was rapidly added to a solution of 9-hexyl-carbazole (5.0 g, 20 mmol) in

dichloromethane (80 mL) with stirring. After cooling to 0ºC, a solution of acetic anhydride (2.04 g, 20 mmol) in 20 mL of dichloromethane was added dropwise over 10 min under vigorous stirring. After stirring overnight at room temperature, a large amount of water and HCl was added into the mixture and extracted with dichloromethane twice, and then washed by 1M aqueous solution of $NaHCO_3$ and water. The combined organic phase was dried over anhydrous $MgSO_4$ and then filtered. The organic solvent was completely removed by rotary evaporation. The residue was purified by column chromatography using petroleum ether and ethyl acetate as eluent to give the purified 3-acetyl-9-hexyl-carbazole. (ESI-MS: [M + H]$^+$ m/z 280.16. Anal. Calc. for $C_{19}H_{21}NO$: C 81.68, H 7.58, N 5.01 %; found C 81.72, H 7.78, N 4.90 %).

In the next step, 0.9 g of 3-acetyl-9-pentyl-carbazole (3.2 mmol) was dissolved in 4 mL anhydrous t-BuOH and 4 mL THF. After cooling to 0 ºC, 2.1 g of t-BuOK (18.75 mmol) was added dropwise, and then the obtained mixture was stirred for 15 min at 0 ºC. Next, 3.7 mL of ethyl trifluoroacetate (4.4 g, 30 mmol) was added and kept stirring at room temperature for 24 h. Then, 3M aqueous solution of HCl was added to the mixture to adjust the pH to be acidic, the resulting mixture was extracted with ethyl acetate, and the organic layer was collected. The organic layer was washed with water and $NaHCO_3$ and dried over anhydrous $MgSO_4$. After the removal of solvent, the obtained residue was purified by silica column chromatography using petroleum ether to give the yellowish solid. For $C_{21}H_{20}F_3NO_2$, ^{1}H NMR (400 MHz, CDCl$_3$, Me$_4$Si): 15.76 (s, 1H), 8.77 (s, 1H), 8.20 (d, 1H), 8.11 (d, 1H), 7.54-7.58 (m, 1H), 7.46-7.48 (m, 2H), 7.27-7.37 (t, 1H), 6.73(s, 1H), 4.35 (t, 2H), 1.92 (m, 2H), 1.29-1.39 (m, 4H), 0.89 (t, 3H). ESI-MS: [M + H]$^+$ m/z 376.15.
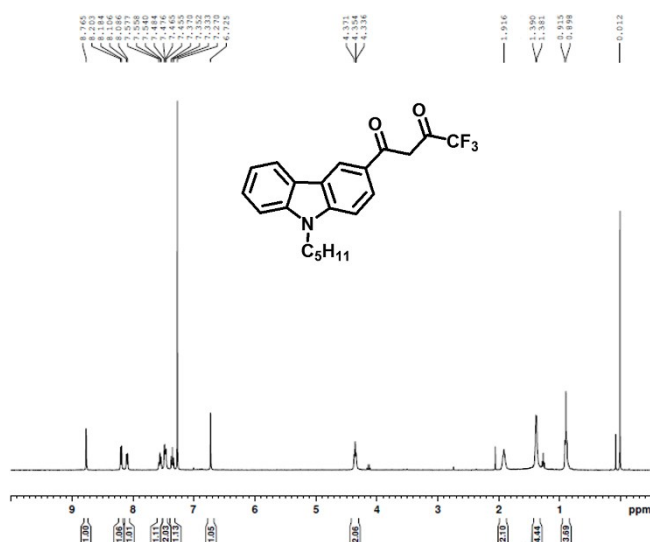
Synthesis of [Eu(THA)₃(phen)]. This complex was prepared by the conventional method.[S1] A solution of HTHA (541.6 mg, 1.5 mmol) and phen (99.1 mg, 0.5 mmol) in EtOH (15 mL) was neutralized with 1.5 mL aqueous NaOH solution (1 M), followed by a dropwise addition of an aqueous solution of $Eu(NO_3)_3 \cdot 6H_2O$ (223.0 mg, 0.5 mmol). Then, the mixture was stirred at 80 ºC for 12 hours. The precipitated product was filtered and washed by water. The product was dried at 60 ºC in vacuum for 12 hours. Elem. Anal. Calcd.: C, 61.77; H, 4.70; N, 4.80; Eu, 10.42. Found: C, 61.86; H, 4.66; N, 4.79; Eu, 10.35.
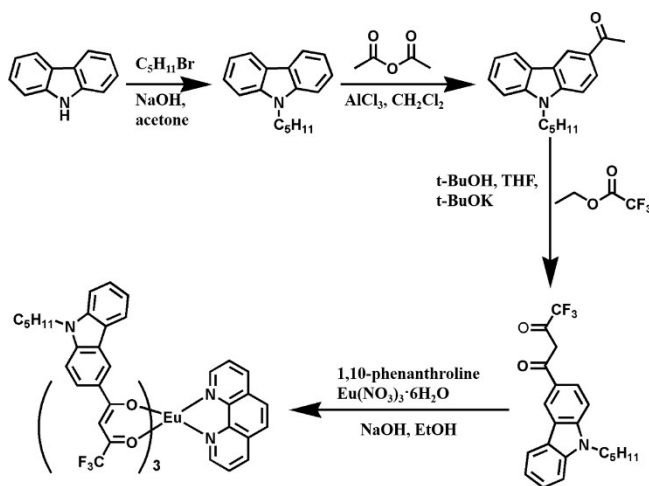
Synthesis of gold nanotriangles (AuNTs). The AuNTs were synthesized via the seed mediated growth protocol as originally proposed.[S2] The initial seeds were prepared by the standard $CTAC/NaBH_4$ procedure: 0.05 M $HAuCl_4$ solution (25 μL) was added to 4.7 mL of 0.1 M CTAC solution, and a freshly prepared 0.01 M $NaBH_4$ solution (300 μL) was then injected under vigorous stirring. Excess of borohydride was consumed

by keeping the seed solution for 2 h at room temperature prior to use to achieve seed@CTAC solution. Then, in a typical synthesis, 40 mL AuNTs solution were prepared from the following two growth solutions: 1) 1.6 mL of 0.1 M CTAC solution was added to 8 mL of Milli-Q water, followed by 40 μL of 0.05 M $HAuCl_4$ and by 15 μL of 0.01 M NaI solutions (designated as solution 1); 2) 500 μL of 0.05 M $HAuCl_4$ solution was added to 40 mL of 0.05 M CTAC, followed by 300 μL of 0.01 M NaI solution (designated as solution 2). The first solution was used to grow the CTAC capped seed into larger nanoparticles, while the second one was used as the NTs growth batch. Before proceeding, the initial seed@CTAC solution was diluted tenfold in a 0.1 M CTAC solution. Subsequently, 40 μL and 400 μL of 0.1M AA solutions were added to solutions 1 and 2 respectively, and both solutions were manually stirred until their complete transparency was achieved, indicating the reduction Au(III) to Au(I). Finally, 100 μL of diluted seed@CTAC solution was added to solution 1 (and manually stirred for 1 second), and immediately 3.2 mL of this solution was added to solution 2 (and manually stirred for a few seconds). The AuNTs dispersion was left undisturbed at room temperature for at least 1 hour. We observed that addition of 15 μL of 0.01 M NaI solution to solution 1 further improved the yield of NTs obtained via the fast-addition procedure. After spectroscopic characterization, the AuNTs dispersion was purified by addition of a selected amount of 25 wt% CTAC solution. Flocculation of the AuNTs was completed overnight, the supernatant was then removed and the precipitated particles were redispersed in 5 mL of 0.1 M CTAC solution. Typically the concentration of Au(0) in the purified sample was around 1.75 mM.

Synthesis of Au-phMSNs. Au-phMSNs was prepared by the sol-gel method.[S3] The as-synthesized AuNTs were washed by centrifugation (40 mL aliquots at a time, at 9,500 rpm for 25 min). The residue was diluted to 20 mL by adding water. Then, 200 μL of 0.1 M NaOH solution was added upon stirring. Following this step, three 100 μL injections of 20% TEOS and 4% PTES in methanol were added under gentle stirring at 30 minute intervals. After reaction for 24 h, three 60 μL injections of 20% TEOS in methanol were added under gentle stirring at 30 minute intervals. The

mixture was reacted for 3 days at 26~28 ℃. Then, the as-synthesized Au-phMSNs was washed extensively with methanol to completely remove the residual CTAC.

Synthesis of Au-phMSNs@P(NIPAm-co-MAA) (named as AMP). To functionalize the surface of Au-phMSNs nanospheres, the obtained particles were first modified by excessive amount of 3-(trimethoxysilyl)propylmethacrylate (MPS) to introduce double bond onto the pores and surface of mesoporous silica shell. The desired amount of Au-phMSNs nanoparticles (NPs) was redispersed in 30 mL of pure ethanol and 200 μL of MPS was added dropwise to the dispersion under continuous stirring with a magnetic stirrer. After stirring for 24 h at 30 °C, the dispersion was refluxed for 1 h to ensure covalent binding. Afterwards, the dispersion was cooled to room temperature, washed with ethanol for several times and then dried at 60 °C for 12 h.

Au-phMSNs@P(NIPAm-co-MAA) nanospheres were achieved by a facial photo-induced polymerization. NIPAm (0.125 g), MAA (7.6 μL), and TPO (0.003 g, photoinitiator) were dissolved in 500 μL of 1,4-dioxane to form transparent solution and then 20 mg of Au-phMSNs@MPS NPs were added. The suspension was sonicated for 30 min and further stirred overnight at room temperature in the dark. After that, the resulting monomer-contained NPs were exposed to UV light (200 W/cm^2, LAMP, PHILIPS) for 8 min to get the photoinitiated polymerization. After that, the prepared product was washed with ethanol and water several times to remove unreacted monomers and impurities, then dried in vacuum at 50 °C to obtain the final sample of Au-phMSNs@P(NIPAm-co-MAA) (named as AMP).

Synthesis of Au-phMSNs@P(NIPAm-co-MAA)-cRGD (named as AMPC). cRGD peptide was immobilized onto AMP by using coupling agents (EDC and NHS).[S4] Briefly, EDC (5.0 mg) and NHS (4.6 mg) were added into the above-prepared AMP solution (5.0 mL) and the mixture was stirred at room temperature for 4 h. After the reaction, cRGD (3.1 mg) was added to the activated AMP solution simultaneously and the new mixture was incubated overnight. Subsequently, the solution was centrifuged at 8000 rpm for 15 min. The residual small molecules including EDC,

NHS, and cRGD in the supernatant were discarded. Then, the residue was dried in vacuum at 50 °C to obtain the final sample of Au-phMSNs@P(NIPAm-co-MAA)-cRGD (named as AMPC).

Luminescence functionalization of Au-phMSNs@P(NIPAm-co-MAA)-cRGD by [Eu(THA)$_3$(phen)]. 10 mg of Au-phMSNs@P(NIPAm-co-MAA)-cRGD was dispersed in 10 ml of chloroform, followed by sonication for 30 min. After addition of 5 mg of [Eu(THA)$_3$(phen)], the mixture was continuously stirred for 24 h at 45 °C, followed by filtration and washing with chloroform until no red color emission of the Eu(III) complex was seen from the filtered solution under UV light (365 nm) radiation. The solid was dried at room temperature. And the obtained powder was denoted as Au-phMSNs@P(NIPAm-co-MAA)-cRGD@Eu(THA)$_3$(phen) (nanocomposite).

Preparation of Au-phMSNs@P(NIPAm-co-MAA)@Eu(THA)$_3$(phen) (AMPE). A similar process was employed for preparing AMPE NPs by using pure AMP NPs instead of AMPC NPs as described above.

Loading and release experiments. For DOX loading, nanocomposite samples were mixed with 2 mL of DOX solution (1 mg/mL). After being shaken for 24 h at 45 °C to reach the equilibrium state under dark conditions, the DOX-loaded samples (named as Nanocom-DOX) were collected by centrifugation, whereas the supernatant was collected for UV measurement to determine the adsorbed amount of DOX. Then, Nanocom-DOX samples were immersed in 2 mL of PBS buffer solutions (pH = 7.4 and 5.0) at 37 °C with gentle shaking. At predetermined time intervals, PBS was taken out and replaced with an equal volume of fresh PBS. The amount of released DOX in the supernatant solutions was measured by UV-vis spectrophotometer at a wavelength of 480 nm. The loading and release process of Nanocom-DOX samples were proceeded following the same procedure.

Near-infrared (NIR) was used to activate/heat the Nanocom-DOX to accomplish the DOX release. Suspension of Nanocom-DOX was placed into tubes and treated by NIR (808 nm, 1 W/cm^2). After the treatment, the dosing amount of drug was detected by the luminescence intensity of Eu(III) ions excited at 808 nm. Then, an IR thermal

camera was used to measure the temperature. The supernatant was taken for DOX detection and the dye-leaking of Eu(III) complex measurements.

DOX loaded AMPE NPs (AMPED). For comparison, an experiment of DOX loading into the AMPE NPs without any modification was carried out by using the same method as above.

Synthesis of Eu(THA)$_3$(phen)@DOX. The complex [Eu(THA)$_3$(phen)] (10 mg) was mixed with 10 mL of DOX aqueous solution (1 mg/mL). After being shaken for 24 h at 45 °C to reach the equilibrium state under dark conditions, the Eu(THA)$_3$(phen)@DOX sample was collected by centrifugation. And then we tested the steady-state spectra, fluorescence lifetime, and quantum yield of Eu(THA)$_3$(phen)@DOX and [Eu(THA)$_3$(phen)].

S1.3. Methods and instruments

Powder X-ray diffraction (PXRD) patterns were recorded over the 2θ range of 3-65° using a Rigaku-Dmax 2400 diffractometer with Cu Kα radiation. Elemental analyses were run on an Elementar Vario EL analyzer. The contents of Eu(III) ions were obtained by inductively coupled plasma-atomic emission spectroscopy (ICP) using an IRIS Advantage ER/S spectrophotometer. Dynamic light scattering (DLS) measurements were conducted on Zetasizer Nanoseries (Nano ZS90). The ^{1}H NMR spectra were measured using a Bruker 400 MHz spectrometer in d-trichloromethane with tetramethylsilane [Si(CH$_3$)$_4$] as an internal standard. Fourier transform infrared (FTIR) spectra of the materials were measured within the 4000–400 cm^{-1} wavenumber range by using a Nicolet 360 FTIR spectrometer with the KBr pellet technique. The luminescent spectra of drug release were measured in a PBS buffer on a Hitachi F-4500 spectrophotometer. The steady-state luminescence spectra, lifetime measurements, and overall quantum yields of the samples were recorded using an Edinburgh Instrument FSL920. The steady-state measurements used a 450W Xe arc lamp as the excitation source and the lifetime used Nd-pumped OPO lette laser as the excitation source. Three parallel measurements were carried out for each sample, so that the presented value corresponds to the arithmetic mean value. The errors in the quantum yield values associated with this technique were estimated to be within 10%.

All measurements were carried out at room temperature. The morphological, structural, and chemical characterization of all samples was run at the nano/atomic scale using field emission HRTEM (Tecnai™ G2 F30; FEI Company, USA) working at 120 kV, which was equipped with EDX (AMETEK Inc., USA) and high-angle annular dark-field scanning transmission electron microscopy (HAADF-STEM).

S1.4. Experimental methods

Energy-transfer analysis. The efficiency of energy transfer from [Eu(THA)$_3$(phen)] to the AuNTs was evaluated using Förster analysis:[S5,S6]

$$E = \frac{mk_{D\to A}}{\tau^{-1} + mk_{D\to A}} = \frac{mR_0^6}{mR_0^6 + r^6}$$

(S1)

where $k_{D\to A}$ is the rate of energy transfer, r is the distance between the donor and acceptor, R_0 is the Förster distance, or the distance at which the energy transfer efficiency is 50%, and m is the number of acceptor molecules per donor. This quantity (E) can be measured experimentally:

$$E = 1 - \frac{\tau_{D\to A}}{\tau_D}$$

(S2)

where τ_D is the lifetime of [Eu(THA)$_3$(phen)] alone and $\tau_{D\to A}$ is the lifetime of the AMPE or AMPED. R_0 is determined from the spectral overlap integral:

$$R_0^6 = \frac{9000(\ln 10)k^2 Q}{128\pi^2 N n^4} \int_0^\infty F_D(\lambda)\varepsilon_A(\lambda)\lambda^4 d\lambda$$

(S3)

where κ^2 is the relative orientation factor of the dipoles, taken to be 0.476 for static donor−acceptor orientations,[S7,S8] Q_D is the quantum efficiency of the donor, N is Avogadro's number, n is the index of refraction of the medium, which is taken to be 1.334 for PBS,[S9] $F_D(\lambda)$ is the normalized intensity of the donor, and $\varepsilon_A(\lambda)$ is the extinction coefficient of the acceptor at wavelength λ. The average number of Au attached to [Eu(THA)$_3$(phen)], m, was determined from the optical cross sections of the spectra of [Eu(THA)$_3$(phen)], the AuNTs, and the corresponding assembly.

The average lifetime $<\tau>$ can be calculated using the following equation

$$<\tau> = \frac{\sum A_i \tau_i^2}{\sum A_i \tau_i}$$

(S4)

Where τ_i is the component decay times and A_i is weighed amplitudes.

Two-photon absorb cross-section

TPA cross-sections were determined via a comparative method, by measuring the two-photon excited fluorescence (TPEF) using Rhodamine B as a reference. The fundamental of a mode-locked Ti:sapphire laser (690–850 nm, Tsunami) was focused into a quartz cuvette having an optical geometry, and detected with a liquid-nitrogen cooled charge-coupled device (CCD) (SPEC-10-400 B/LbN, Roper Scientific) attached to a polychromator (Spectropro-550i, Acton). The TPA cross-sections have been measured using the two-photon-induced fluorescence measurement technique with the following equation:[S10]

$$\sigma = \sigma_{ref} \frac{Q_{ref} c_{ref} n_{ref}}{Q} \frac{F}{c} \frac{F}{n} \frac{F}{F_{ref}}$$

(S5)

Here, the subscripts ref stands for the reference molecule, σ is the TPA cross-section value, c is the concentration of solution, n is the refractive index of the solution, F is integrated area of the detected two-photon induced fluorescence signal, and Q is the fluorescence quantum yield.

Cell culture. Prostatic cancer cell lines (PC-3) and bone marrow stromal cells lines (bMSCs) were provided by the Institute of Biochemistry and Cell Biology, SIBS, CAS (China). Cells were cultured in regular growth medium consisting of DMEM/F12 supplemented with 10% FBS (fetal bovine serum) at 37 °C in a humidified and 5% CO_2 incubator. The cells were routinely harvested by treatment with a trypsin-ethylenediaminetetraacetic acid (EDTA) solution (0.25 %).

Cell cytotoxicity assay by MTT protocol. In-vitro cytotoxicity was assessed by the standard MTT assay. The statistical evaluation of data was performed using a two-tailed unpaired Student's t-test. Each data point is represented as mean ± standard deviation (SD) of eight independent experiments ($n = 6$, n indicates the number of

wells in a plate for each experimental condition). The dose dependence of the cytotoxicity was investigated at different particle concentrations. PC-3 cells were seeded in a 96-well plate at a density of 10^5 cells per well and cultured in 5% CO_2 at 37 °C for 24 h. Then, Nanocom-DOX was added to the medium, and the plate was exposed to NIR light (808 nm, 1 W/cm^2) for 0 or 5 min. The cells were incubated in 5% CO_2 at 37 °C for 24 h. At the end of the incubation, the medium was removed, and 100 μL of MTT solution (diluted in a culture media with a final concentration of 0.5 mg/mL) was added and incubated for extra 4 h. The medium was then replaced with 100 μL of dimethyl sulfoxide (DMSO) per well, and the absorbance was monitored using a microplate reader (Bio-TekELx800) at the wavelength of 580 nm. The cytotoxicity was expressed as the percentage of cell viability compared to untreated control cells.

Intracellular observation of the released DOX in PC-3 cells by confocal laser scanning microscopy (CLSM) imaging. For CLSM imaging, the cells were seeded in 12-well culture plates (a clean cover slip was put in each well) and grown overnight as a monolayer. The cells were then incubated with Nanocom-DOX ([DOX] = 25 μg/mL) in 5% CO_2 at 37 °C for 6 h, 12 h, 24 h, respectively. Thereafter, the cells were washed with PBS three times, fixed with 2.5% formaldehyde at 37 °C for 10 min, and then washed with PBS three times again. The cover slips were placed on a glass microscope slide, and the samples were analyzed using CLSM (FV1000).

Competition assay. The PC-3 cells seeded in 35 mm glass microscopy dishes were grown overnight in complete medium. Cells were treated with 20 μL excess of cRGD in serum-free medium (10 μg/mL) for 15 min. The cells were washed with PBS, incubated with Nanocom-DOX and AMPED ([DOX] = 25 μg/mL) for 3 h at 37 °C, and then fixed in solution containing 4% cold paraformaldehyde for 20 min. The cell surface distribution of the NPs was observed using a confocal microscope.

In-vivo X-Ray CT imaging. The Nanocom-DOX ([DOX] = 1 mg/kg) was administered by intravenous injection to nude mice bearing PC-3 tumor (~40 mm^3). Images were acquired before and after injection (24 h) on a Quantum FX (PerkinElmer, Waltham, MA, U.S.A.).

In-vivo TPL imaging. The Nanocom-DOX ([DOX] = 1 mg/kg) was administered by intravenous injection to nude mice bearing PC-3 tumor (~40 mm^3). Images were acquired at 0.5, 1, 2, 4, and 8 hours time of post-injection on an IVIS Spectrum (PerkinElmer, Waltham, MA, U.S.A.), using an excitation wavelength of 808 nm and emission one of 612 nm. During imaging, mice were held under 1−3% inhaled isoflurane anesthesia. Mice were allowed to recover between imaging time points. Images were processed using Living Image software, where ROI's corresponding to the tumor and background signal intensity were used to determine background subtracted radiant efficiency in the tumors.

In-vivo PTI imaging. The Nanocom-DOX ([DOX] = 1 mg/kg) was administered by intravenous injection to nude mice bearing PC-3 tumor (~40 mm^3). After injection at 0, 0.5, 1, 2, 4, and 8 h time, the tumors were irradiated by NIR laser (808 nm, 1 W/cm^2) for 5 min. Images were acquired on a Ti90 thermal imager (Fluke, U.S.A.).

Therapeutic efficacy evaluation of the nanocomposite. PC-3 tumor model for therapy evaluation was established by subcutaneously inoculating PC-3 cells (~8×10^6) into the nether axillary fossa in the nude mice. The mice were investigated after 7 days of inoculating. After the tumors had developed to about 40 mm^3, the tumor-bearing mice were randomized into six groups (four mice in each group) and were treated by tail vein injection with PBS with NIR irradiation, nanocomposite, free DOX with NIR irradiation, Nanocom-DOX, nanocomposite with NIR irradiation and Nanocom-DOX with NIR irradiation ([DOX] = 1 mg/kg). For systemic injection experiments, a 200 μL of each above-mentioned solution was administered through the tail vein. After post-injection (1 h), four sets of mice were irradiated by NIR laser (808 nm, 1 W/cm^2) for 5 min. The tumor volume and body weight of each mouse were monitored every two days after NIR laser (808 nm, 1 W/cm^2) irradiated for 5 min during 20 days. The tumor volume was calculated as length×(width)^2×1/2 with a caliper.

S2. Design of Multifunctional Nanocomposite

Scheme 1 shows the structure and working principle of the theranostic nanocomposite. The two-photon-sensitized Eu^{3+} complex, [Eu(THA)$_3$(phen)], was selected as the donor on the basis of the following considerations: (1) the exchangeable and extendable coordination sphere of Eu^{3+} can attract drug molecules gathered around the complex, (2) the excellent luminescent properties of the complex, including higher resolutions, long lifetimes, lower photodamage and photobleaching, can be used for long-term monitoring dynamics of drug release in real-time, (3) the relatively low toxicity of the complex to cells and living organisms can fulfil clinical applications,[S1,S11,S12] and (4) the laser-induced heating effect, especially for biological tissues, is expected to be significantly minimized by the excitation wavelength of 808 nm.[S13] Most importantly, the emission peaks of [Eu(THA)$_3$(phen)] overlap the localized surface plasmon resonance (LSPR) band of AuNTs (500-750 nm),[S2] which determines the ability to achieve the LRET process.

Considering the relatively poor stability of Eu^{3+} complexes under moisture conditions, we designed multifunctional AuNTs core/phenyl mesoporous silica shell NPs (designated as Au-phMSNs) and constrained the [Eu(THA)$_3$(phen)] by strong π-π interactions and the hydrophobic property to achieve the LRET and avoid fluorescence-quenching and leakage of the complex. Thus, this nanoplatform fulfills the requirements of the real-time drug release monitoring without the need for light-absorbing drugs, as well as may simultaneously achieve synergistic photothermal chemotherapy that is activated by 808 nm, based on the LRET process.

To achieve the targeted cancer therapy and smart drug release, cyclic (Arg-Gly-Asp-D-Phe-Lys) (cRGD) and pH/thermo-coupling sensitive polymer brushes, poly[(N-isopropylacrylamide)-co-(methacrylic acid)] (P(NIPAm-co-MAA)), were introduced into the NPs. Additionally, the prototype of this novel theranostic nanocomposite, (Au-phMSNs@P(NIPAm-co-MAA)-cRGD@Eu(THA)$_3$(phen)), was developed for the simultaneous monitoring of the pH/NIR-triggered drug release and synergistic photothermal chemotherapy.

It is known that LRET will diminish as the distance between the donors and acceptors is extended. As shown in Scheme 1, when the drug molecules are added, the distance is extended because most of the drug molecules become directly gathered around the Eu^{3+} complex via a coordination interaction; in turn, the distance is shortened upon the drug release. Such a change in the distance made the LRET convertible, leading to a change in AuNTs' photothermal conversion efficiency and Eu^{3+} luminescence. Sequentially, the dual-mode real-time drug release monitoring by PTI and TPL imaging can thus be achieved, based upon the temperature and emission intensity. One significant advantage of this nanocomposite is that the drug release can be quantitatively monitored both in-vitro and in-vivo using an IR thermal camera. We believe this technique can be readily translated from mice to humans. Thus, based on this design, multi-mode imaging and real time monitoring of drug release, the synergistic photothermal chemotherapy of the nanocomposite can be triggered by the same NIR excitation wavelength.

S3. Characterization of Nanocomposite
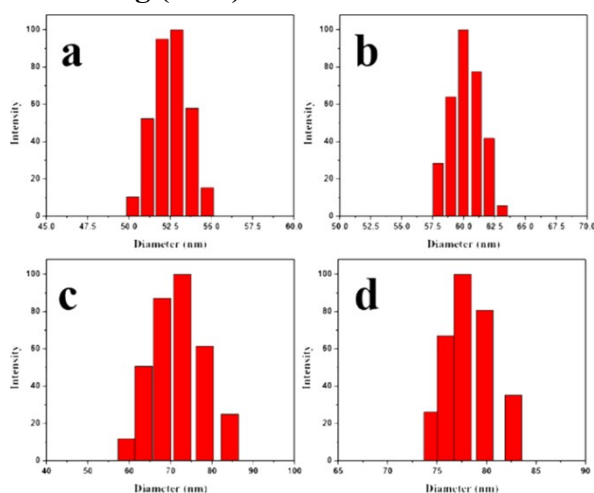
S3.1 Dynamic light scattering (DLS)

Figure S1. DLS plots of (a) AuNTs, (b) Au-phMSNs, (c) AMP, and (d) nanocomposite.
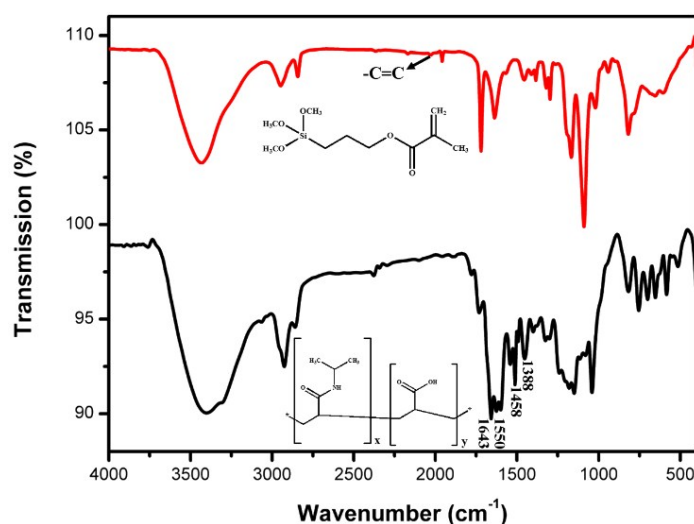
S3.2. FT-IR spectra

Figure S2. FT-IR spectra of Au-phMSNs@MPS (red) and AMP (black).

Fourier transform infrared (FTIR) spectra also provided clear evidence for the formation procedure of the AMP (Figure S2). In the case of the MPS-modified core-shell nanoshpere, the presence of C=O stretching at 1720 cm^{-1} and -CH$_2$ stretching at 2958 cm^{-1} (Figure S2, red line) indicates the successful functionalization.[S14] In the spectrum of AMP (Figure S2, black line), the appearance of characteristic IR peaks at 1643 and 1550 cm^{-1} should be assigned to the secondary amide C=O stretching and N-H bending vibrations, respectively. In addition, the band at 1458 cm^{-1} corresponds to the bending vibration of C-H, while the band at 1388 cm^{-1} is attributed to the deformation of methyl groups on –C(CH$_3$)$_2$ belonging to the characteristic peaks of PNIPAm. These results confirmed the successful copolymerization of NIPAm with MAA onto the Au-phMSNs, while the rough surfaces of the AMP NPs were clearly observed in Figure 1c.

Finally, AMP was further conjugated with a targeting peptide (cRGD) to form Au-phMSNs@P(NIPAm-co-MAA)-cRGD (named as AMPC). The surface charge of the prepared materials was investigated using zeta potential (ζ) analysis. The charge of the AMP (-33.7 mV) was shifted to a positive direction (to -22.1 mV) upon conjugation with the hydrophilic peptide, cRGD, thus indicating that cRGD molecules are present on the surface of the AMP NPs.[S15-S18]
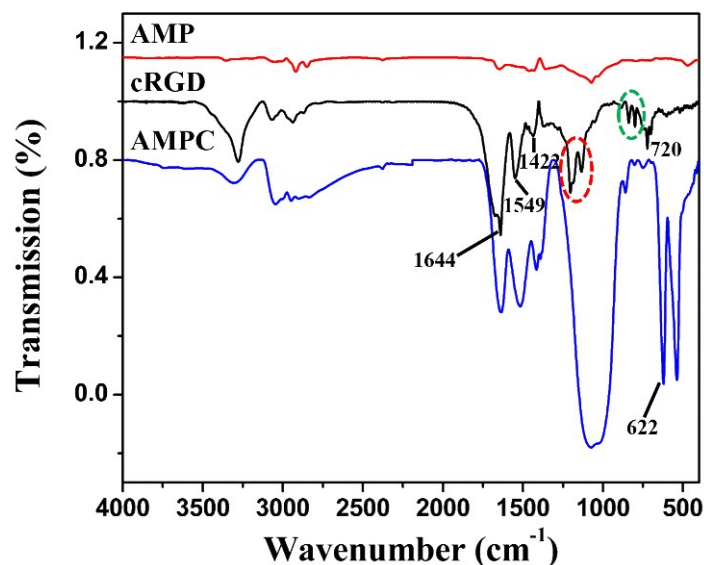
Figure S3. FTIR spectra of AMP (red), AMPC (blue), and cRGD (black).

As seen in Figure S3, cRGD displays three special peaks of amide bands I ($\nu_{C=O}$,1690-1640), II (ν_{N-H}, 1550-1500), and Ⅲ (ν_{C-N}, 1420-1400) at 1644 and 1550, 1422 cm^{-1}, respectively.[S19] These bands are similar to the polymer P(NIPAm-co-MAA) due to the amido bond that also exists in PNIPAm.[S20] Hence, the cRGD-conjugated NPs and P(NIPAm-co-MAA) modified Au-phMSNs both possess the three characteristic bands. However, if we observe carefully, the relative intensities between the two peaks (bands I and II) have changed in the cRGD-conjugated NPs. In addition, the bands of stretching vibrations of C-O appearing at 1190 and 1140 cm^{-1} (red loop) that are present in cRGD also appear in the cRGD-conjugated NPs. At the same time, as the other bands, the out-of-plane bending of C-H of mono-substituted benzene (green loop) (800, 830 cm^{-1}) and $(CH_2)_n$ (n$\geqslant$4) (720 cm^{-1}), belonging to phenylalanine and lysine in cRGD, respectively, also appear in the cRGD-conjugated NPs. The shifts of the two bands toward lower wavenumber may be attributed to the susceptible bending vibration in fingerprint region. In conclusion, we believe that the cRGD has been linked onto the NPs, as confirmed by the zeta potential and FTIR data.
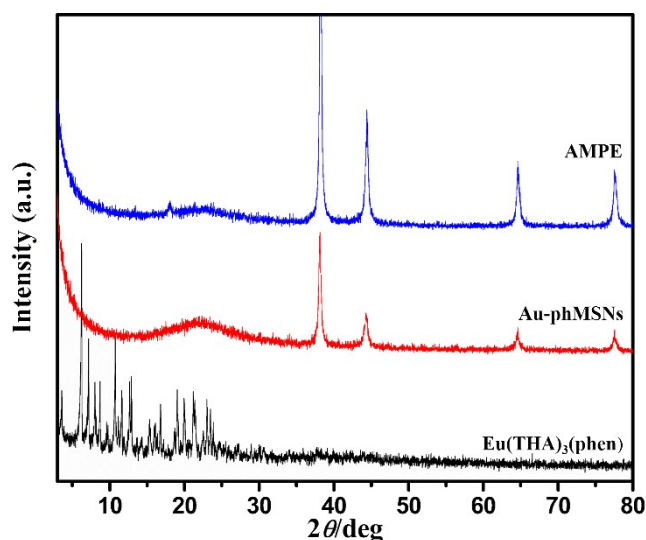
S3.3. Powder X-ray diffraction (PXRD) patterns

Figure S4. PXRD patterns of [Eu(THA)$_3$(phen)] (black), Au-phMSNs (red), and AMPE (blue).
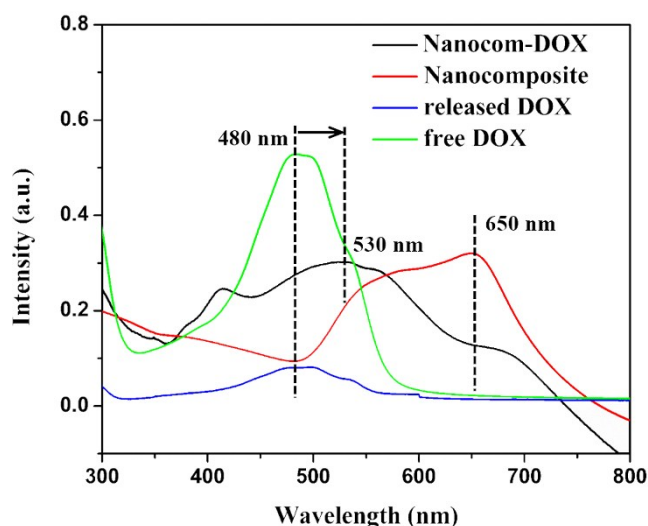
S3.4. UV-vis spectra

Figure S5. UV−vis spectra of the free DOX, nanocomposite, Nanocom-DOX, and released DOX in PBS buffer (pH = 7.4) at room temperature.

DOX was chosen as the model drug to evaluate the drug loading and release properties; a DOX-containing nanocomposite (abbreviated as Nanocom-DOX) was prepared. Due to its special structure, DOX could be encapsulated into the phenyl-modified channels of the Au-phMSNs. This encapsulation is driven by the coordination effect with the Eu^{3+} ions, hydrophobic interactions, and π-π stacking. The final drug loading content in the Nanocom-DOX was found to be 26.1% with a high loading efficiency of up to 82.4%. The UV-vis spectra showed that the intensity

of the characteristic absorption peaks of DOX significantly decreased in the solution after loading into the nanocomposite, indicating that most of the DOX molecules were directly clustered into the phenyl-modified mesoporous silica (Figure S5).

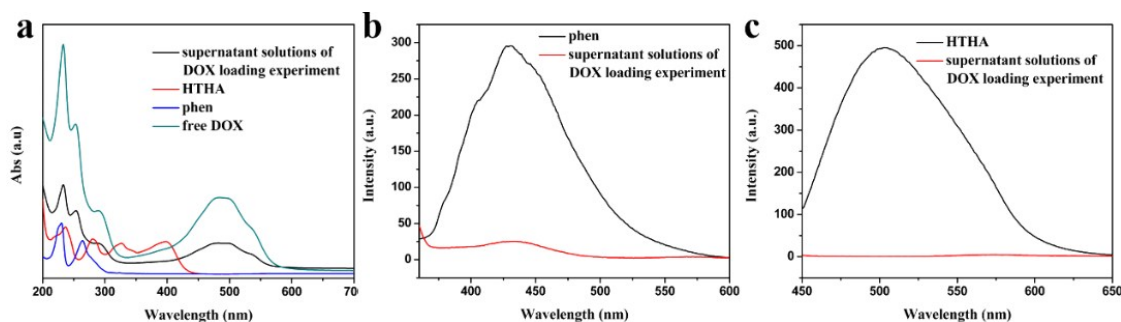## S4. Photophysical Properties

Figure S6. (a) UV−vis spectra of the free DOX, HTHA, phen, and the supernatant solution in the DOX loading experiment at room temperature. (b) Emission spectra of phen (black), supernatant solution in DOX loading experiment (red) (λ_{ex} = 350 nm). (c) Emission spectra of HTHA (black), supernatant solution in DOX loading experiment (red) (λ_{ex} = 440 nm).

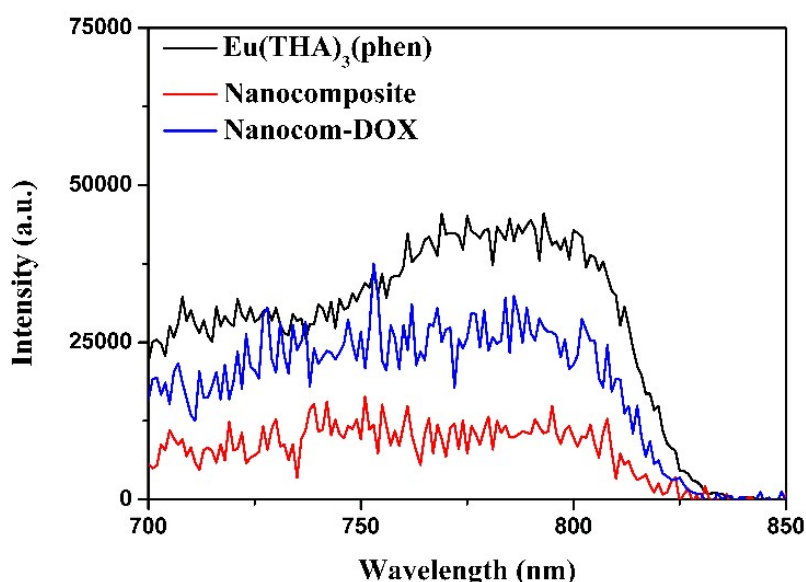**Figure S7.** TPL excitation spectra of [Eu(THA)$_3$(phen)] (black), nanocomposite (red), and Nanocom-DOX (blue) in PBS buffer (pH = 7.4).

To further confirm whether the [Eu(THA)$_3$(phen)] complex stays integrated into the nanomaterial after the DOX loading, the supernatant solution in the DOX loading

experiment was collected for observing a possible presence of THA and phen moieties. As shown in Figure S6, there were no absorption and emission pearks of the free THA in the supernatant, alghough a slight emission peak of phen was detected. Based on these data, we believe that the THA ligand was not displaced during the DOX loading, which is explained by a strong nature of the Eu-O bond. Figure S7 reveals that the location of the TPL excitation peaks has hardly any change between both nanocomposite and Nanocom-DOX, thus further suggesting that the chromophore of the Eu^{3+} complex did not change, and DOX did not displace the THA ligand.

To further ascertain the interaction between DOX and Eu^{3+} ions, the $^5D_0$ emission decay curves were monitored at 613 nm under the excitation wavelength that maximized the emission intensity. All these curves can be fitted by bi-exponential functions, indicating two kinds of symmetrical site of Eu^{3+} ion. The fitting data are presented in Table S1, including lifetime values of $^5D_0$ levels of Eu^{3+} ions, and the corresponding relative weightings for each species and the average lifetime $<\tau>$.

To study the coordination environment surrounding Eu^{3+} ions, especially the influence caused by vibrations of water molecules, it is possible to estimate the number of water molecules (n_w) coordinated to the Eu^{3+} ions in the hybrid hosts by using the empirical formula of Supkowski and Horrocks:[S21]

$$n_w = 1.11(k_{nr} - k_r - 0.31)$$
(S6)

It should be noted that the n_w values do not represent a single molecule here since the [Eu(THA)$_3$(phen)] contain two or three local environments of Eu^{3+} ions, but they are considered as a whole.

We propose that the average lifetime ($<\tau>$), radiative (k_r), and nonradiative (k_{nr}) transition rates may be related through the following equation:

$$k_r + k_{nr} = \frac{1}{<\tau>}$$
(S7)

Table S1. Photoluminescence data of [Eu(THA)$_3$(phen)], and Eu(THA)$_3$(phen)@DOX.

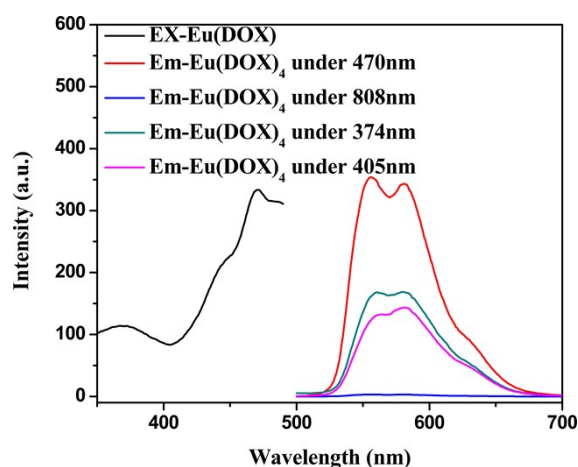|	[Eu(THA)$_3$(phen)]	Eu(THA)$_3$(phen)@DOX
τ_1	0.469 ms (21.59%)	0.270 ms (3.57%)
τ_2	0.581 ms (78.41%)	0.547 ms (96.43%)
$<\tau>$	0.557 ms	0.538 ms
k_r (ms^{-1})	0.62	0.91
k_{nr} (ms^{-1})	1.18	0.95
n_w	0.28	0

Figure S8. Excitation spectrum of [Eu(DOX)$_4$] (black) (λ_{em} = 613 nm). Emission spectra of [Eu(DOX)$_4$] (red, turquoise, pink) (λ_{ex} = 470, 374, and 405 nm, respectively), and TPL emission spectrum of [Eu(DOX)$_4$] (blue) (λ_{ex} = 808 nm).
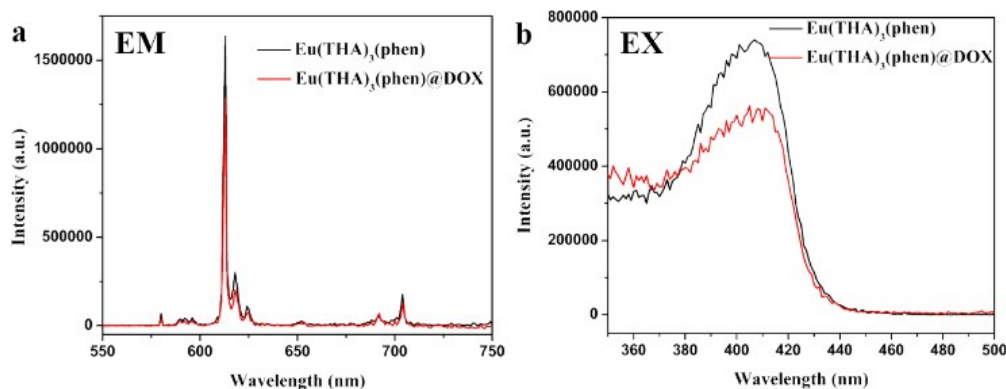

Figure S9. (a) TPL emission spectra of [Eu(THA)$_3$(phen)] (black) and Eu(THA)$_3$(phen)@DOX (red) (λ_{ex} = 808 nm). (b) Excitation spectra of [Eu(THA)$_3$(phen)] (black) and Eu(THA)$_3$(phen)@DOX (red) (λ_{em} = 613 nm).

To further clarify the interaction between the Eu^{3+} complex and DOX, the [Eu(DOX)$_4$] derivative was also synthesized (it was prepared from DOX and

EuCl$_3$·6H$_2$O following the literature method[S22]) and its luminescent properties have been thoroughly investigated. As shown in Figure S8, the maximum and the secondary excitation wavelengths (λ_{ex}) of the [Eu(DOX)$_4$] complex are 470 nm and 374 nm, respectively. Excitation at the two wavelengths yields two broad emissions with the maximum at 556 nm and 580 nm,[S23] corresponding to DOX itself rather than to the characteristic emission peaks of Eu^{3+} ion. For further excluding the interference, we also investigated the luminescence of the [Eu(DOX)$_4$] complex at the excitation wavelengths of 405 nm and 808 nm, respectively. The obtained results revealed that there are weak emission peaks of DOX observed at the 405 nm excitation, but there are no emission peaks observed at the 808 nm excitation. Therefore, DOX can coordinate to Eu^{3+} ion but cannot sensitize the Eu^{3+} ion.

As shown in Table S1, we deduced that the coordinated water molecules in the [Eu(THA)$_3$(phen)] complex were removed from the first coordination sphere of Eu^{3+} after the introduction of DOX molecules, whereas the THA and phen ligands remain coordinated (for details, see also the above discussion of Figure S6). Although Figure S9 shows that the addition of DOX induced a moderate weakening of the emission and excitation intensities of the Eu^{3+} complex, the location of the excitation peaks has not changed at all. The weaker emission intensities of Eu(THA)$_3$(phen)@DOX might indicate a slight loss of the big rigid ligand (phen), which can enhance the absorption of the Eu^{3+} ternary complex,[S24] and the quenching of high-frequency photon vibrations from the DOX molecule.[S25] In addition, the high steric hindrance of DOX also suggests that it is hard to form a strong coordination interaction with Eu^{3+} ions; thus, most of the DOX molecules were gathered around the outer coordination sphere of Eu^{3+} by electrostatic interactions and π-π stacking. Furthermore, based on previous reports on the formation of complexes between a β-diketone ligand and rare-earth ions in alkaline media,[S24] it could be concluded that the C-protonation of THA is achieved only under the strong acidic conditions and, therefore, DOX cannot displace the THA ligand during the chelation process in neutral aqueous environment system. Thus, after the DOX loading into the pores of the phenyl-modified mesoporous silica, most of the DOX molecules were located at the outer coordination sphere of Eu^{3+} ions by

electrostatic interaction and π-π stacking, and the other part of DOX molecules replaced water molecules and a minor amount of phen in the first coordination sphere of Eu^{3+}.

Finally, from the above discussion it is evident that the emission center of Eu^{3+} was not changed after the DOX coordination to Eu^{3+}, even though water and a minor quantity of phen ligands were displaced. Because both DOX and phen have no the ability to sensitize the Eu^{3+} under 808 nm, the total photoluminescence properties cannot be influenced except the intensity decrease. For the control experiment, we can deduce that our design idea is correct because the photoluminescence intensity was enhanced in Nanocom-DOX, thus attributed to the blockage of LRET doubtless.

In order to exclude the luminescence quenching of the Eu^{3+} complex from the influence of mesoporous structure, the contrast experiments on phMSNs without the AuNTs core were conducted. As shown in Figure S10b, the emission intensities of the Eu^{3+} ions remain almost unchanged when the Eu^{3+} complex was loaded into the mesopores of phMSNs. This phenomenon indicates that the change in the emission intensities of the Eu^{3+} ions was attributed to the LRET from the Eu^{3+} complex to AuNTs when the Eu^{3+} complex was loaded into the mesopores of Au-phMSNs.
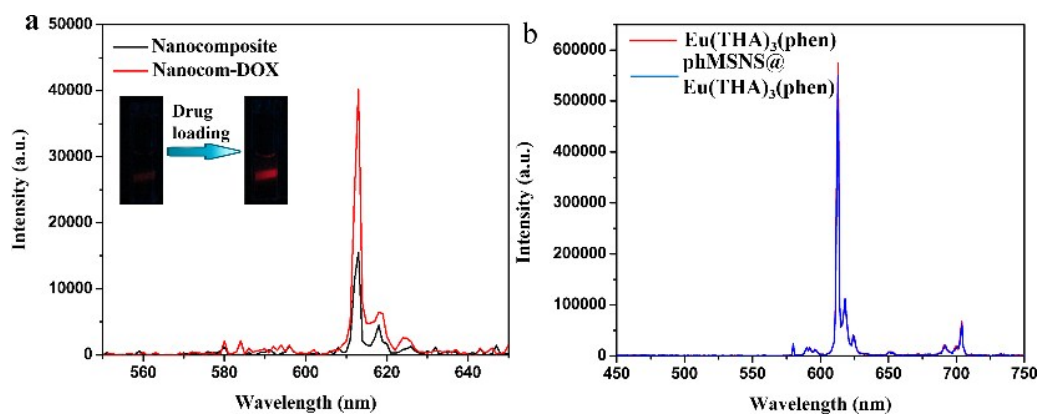

Figure S10. (a) TPL emission spectra of nanocomposite (black) and Nanocom-DOX (red) in PBS buffer (pH = 7.4) at room temperature (λ_{ex} = 808 nm). Inset images show the corresponding change in the luminescence intensity of the NPs solution under a NIR laser (808 nm, 1 W/cm²). (b) TPL emission spectra of [Eu(THA)₃(phen)] (red) and phMSNs@Eu(THA)₃(phen) (blue) in PBS buffer (pH = 7.4) at room temperature (λ_{ex} = 808 nm).

Table S2. Photoluminescence data of the isolated [Eu(THA)₃(phen)], AMPE, and AMPED in PBS buffer (pH = 7.4) at room temperature.

	[Eu(THA)$_3$(phen)]	AMPE	AMPED
τ_1 (ms)	0.392 (18.50%)	0.241 (13.33%)	0.232 (6.30%)
τ_2 (ms)	0.571 (81.50%)	0.523 (86.67%)	0.530 (93.70%)
$<\tau>^a$ (ms)	0.538	0.485	0.511
Q (%)	41.39	3.87	6.49
E^b (%)		9.82	5.05
r^c (%)		1.85	3.55

[a] Calculated using Eq. S4. [b] Calculated using Eq. S2. [c] Calculated using Eq. S1.

The energy-transfer efficiency of AMPE is only 9.82%. This result might be attributed to the following reasons. First, the Eu^{3+} complex exhibits line-like emissions which lead to a lower spectral overlap integral. Second, the Eu^{3+} complex is uniformly distributed in the nanocomposite, whereas some amount of the Eu^{3+} complex is absorbed on the surface of mesoporous silica shells. Thus, only a part of the Eu^{3+} complex can transfer energy to AuNTs. Even though the low energy-transfer efficiency is observed, it was enough to realize all functions in the whole experiment.
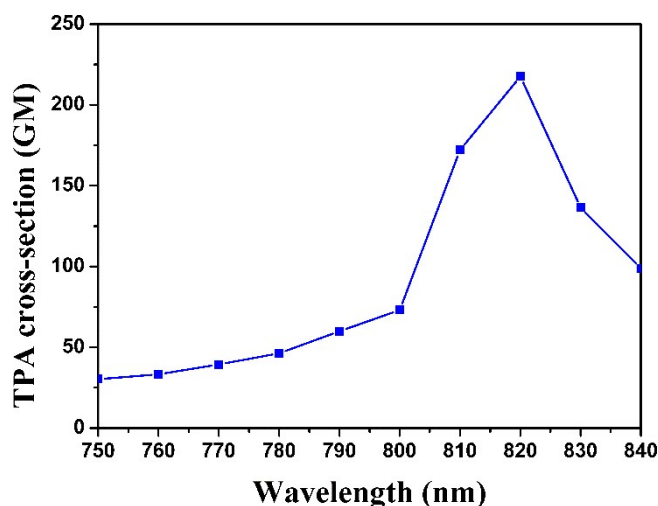

Figure S11. TPA cross sections (σ) for [Eu(THA)$_3$(phen)].

The excitation power dependence was examined in the 750–840 nm range and used in the subsequent determination of the TPA cross-sections (σ), which shows that the [Eu(THA)$_3$(phen)] complex is considered to have high efficiency in two-photon sensitization (Figure S11). The TPE cross sections of the Eu^{3+} complex attain 172.16 GM under 810 nm. The TPE cross sections of the Eu^{3+} complex is rather high,

allowing to achieve an efficient TPE using a relatively low power density cw excitation (~1W/cm^2).
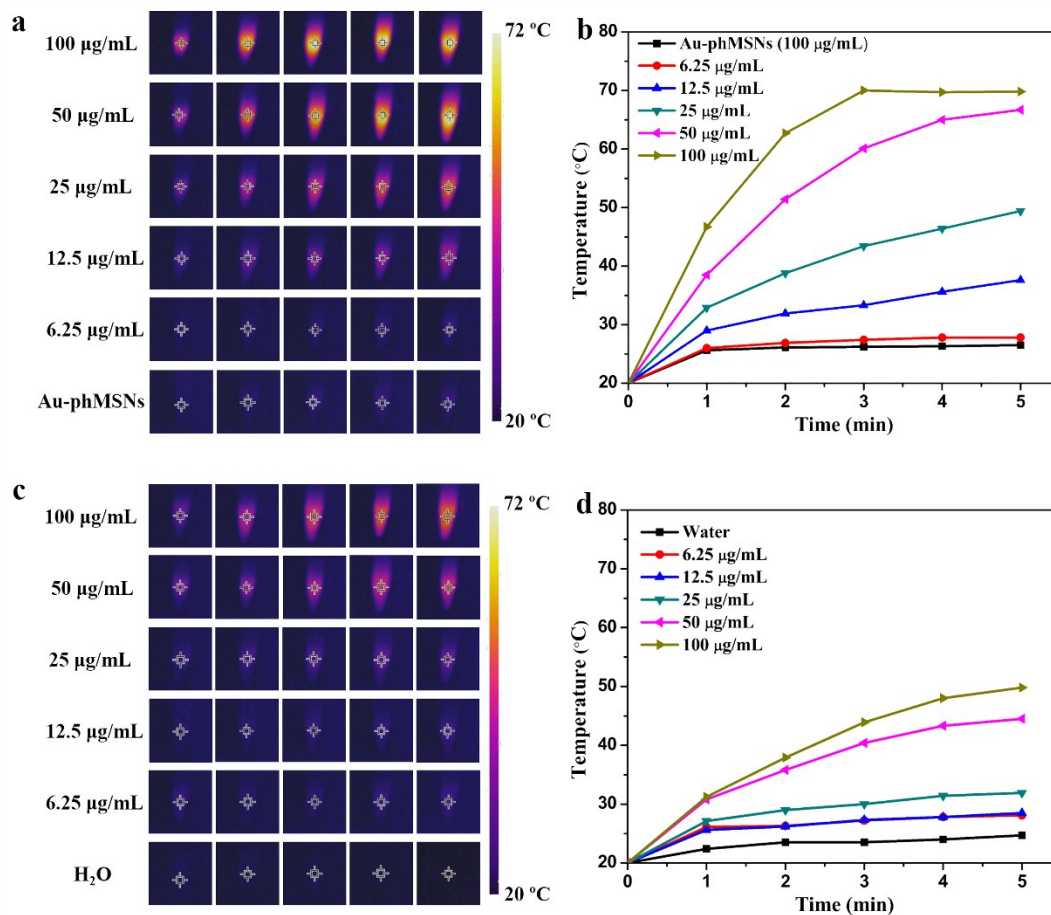
S5. Photothermal Heating Effect

Figure S12. (a) The temperature images of nanocomposite suspension under NIR laser (808 nm, 1 W/cm^2) irradiation; these were recorded by an IR camera at different concentrations. (b) The rate of temperature rise and the final temperature of nanocomposite were proportional to NPs concentration at the constant laser function power (808 nm, 1 W/cm^2). (c) The temperature images of the Nanocom-DOX suspension under NIR laser (808 nm, 1 W/cm^2) irradiation; these were recorded by an IR camera at different concentrations. (d) The rate of temperature rise and the final temperature of Nanocom-DOX were proportional to NPs concentration at the constant laser function power (808 nm, 1 W/cm^2).

Once we confirmed the LRET behavior of the nanocomposite, the next step was to utilize its LRET properties for the NIR photothermal heating. When irradiated by an 808 nm NIR laser at a power intensity of 1 W/cm^2, the solution temperature exceeded

70 °C within 5 min when using a nanocomposite concentration of 100 μg/mL (Figure S12a and S12b). However, insignificant heating with a temperature rise of only ∼5 °C was observed for Au-phMSNs even under long exposure. This provides an additional evidence for the LRET process from [Eu(THA)$_3$(phen)] to the AuNTs. Moreover, the nanocomposite exhibited a laser power intensity-dependent and concentration-dependent photothermal heating effect (see Figures S13 and S12b). These nanocomposite properties will be beneficial for the controllable photothermal therapy.

The NIR photothermal heating efficiency diminished upon the DOX loading into the mesopores of the nanocomposite (Figures S12c and S12d). Thus, the NIR photothermal heating efficiency is an additional piece of evidence that the DOX loaded into the mesopores results in an increased distance between [Eu(THA)$_3$(phen)] and the AuNTs core. Predictably, a corresponding increase in the NIR photothermal heating efficiency was observed upon release of DOX. Simultaneously, a synergistic therapeutic effect is anticipated by the produced thermal effect, which is induced by the enhancement of the DOX release.
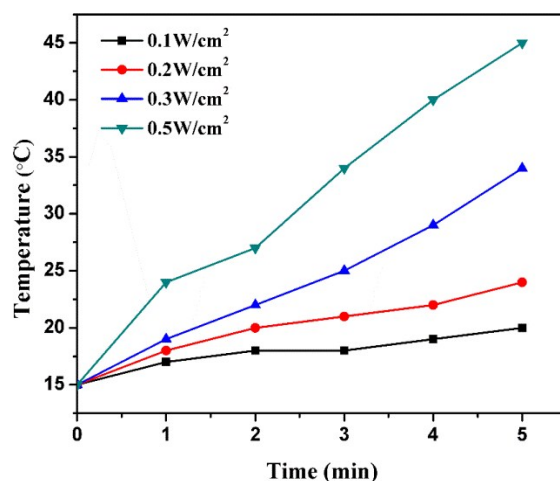

Figure S13. Photothermal heating curves of nanocomposite solution (100 μg/mL) under 808 nm laser irradiation at various power densities for 5 min.

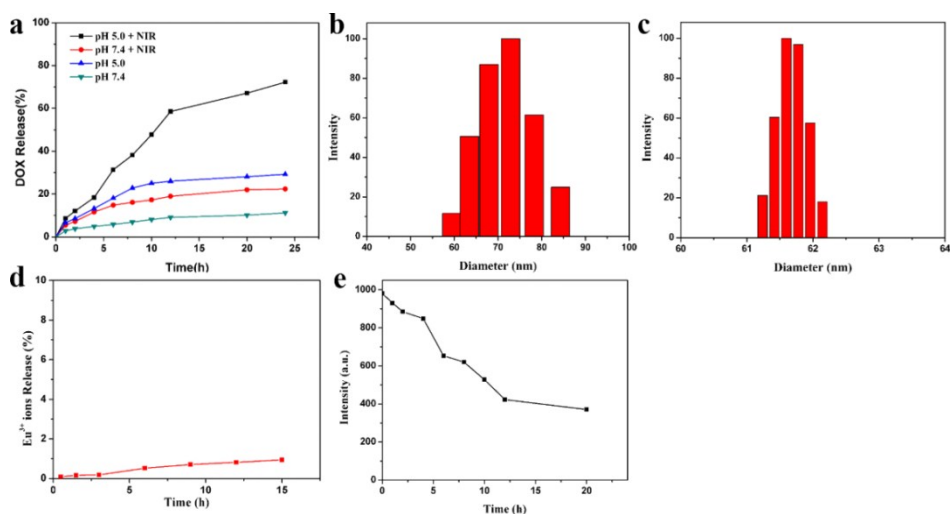## S6. Drug Loading and Release of Nanocom-DOX

Figure S14. (a) DOX release profiles from Nanocom-DOX with or without NIR laser irradiation at different pH values. (b, c) DLS analysis of Nanocom-DOX before (b) and after (c) the drug release. (d) Dye-leaking of the Eu(III) complex as a function of release time at 37 °C under pH 5.0; this was determined from the luminescence intensity of the signals at 612 nm. (e) Linear correlation between the release time and the change in the TPL intensity of the signals at 612 nm of Nanocom-DOX.

To further investigate the drug release properties of the Nanocom-DOX stimulated by the NIR irradiation, we performed additional experiments. These show that the 808 nm NIR irradiation enhanced the cumulative release of DOX at different time points and pH values (Figure S14a) due to the heat stimulated shrink of the P(NIPAm-co-MAA) brushes and weakening of the interactions between DOX and the nanocomposite. As the temperature increased above the low critical solution temperature of P(NIPAm-co-MAA) (37°C),[S26] the polymer chain was forced to shrink to open the porous channels and enable the entrapped drug molecules to leak out. As shown in Figures S14b,c, the hydrodynamic size of the Nanocom-DOX shrunk to 61 nm from the initial value of 72 nm during the process. The release of DOX also exhibited a pH-responsive pattern (Figure S14a), whereas a higher cumulative DOX release was achieved at a lower pH. This can be attributed to the dissociation of electrostatic interactions between the DOX and the polymer shell.[S27] It has been reported that the tumor microenvironment is mildly acidic with a pH range of 5.8 to

7.1,[S28] and the intracellular environment is even more acidic having a pH~5.0.[S29] Most importantly, NIR irradiation significantly affects the controlled DOX release. Taking pH 5.0, for example, the cumulative release of DOX (72.2%) with NIR irradiation was approximately 2.5-fold greater than that without the NIR irradiation (29.2%) (Figure S14a). Thus, the photothermal effect of the nanocomposite could significantly increase the sensitivity and efficiency of the chemotherapy. The pH-sensitive and NIR-stimulative release of DOX can significantly enhance the therapeutic effect, based on the targeting accumulation of the nanocomposite within the malignant prostate gland.[S30]

We analyzed the concentrations of the Eu^{3+} ions in the solutions at different time points (Figure S14d) and found that less than 1% of the Eu^{3+} ions leaked from the Nanocom-DOX during the drug release process. The results suggest that the strong and stable interaction between the Eu^{3+} complex and the phenyl-modified silica pores excludes the possibility of Eu^{3+} leakage during the drug release process. The reason for the negligible Eu^{3+} complex leakage can be attributed to the super hydrophobicity of pores and strong π-π stacking interaction with phMSNs. Moreover, as shown in Figure S15, there is no absorption of free THA and phen in the supernatant solution after the DOX release, suggesting that the original complex was not destructed in this weakly acidic environment.
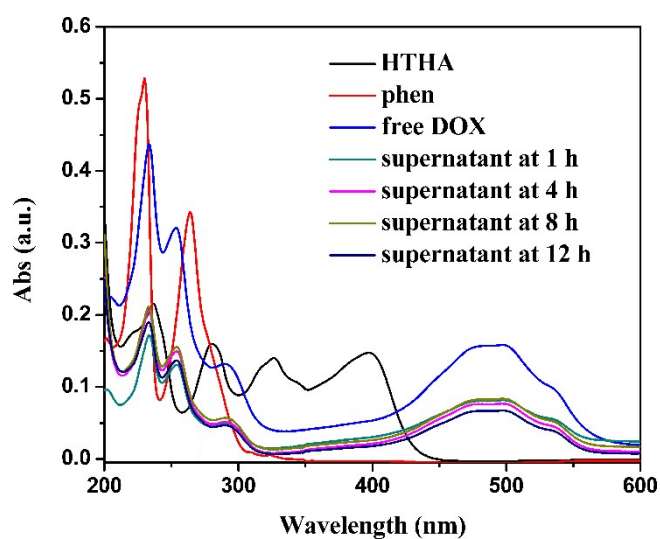

Figure S15. UV−vis spectra of free DOX, HTHA, phen, and the supernatant solution after the DOX release experiment with NIR laser irradiation at 1 h, 4 h, 8 h, and 12 h in PBS buffer (pH = 5.0).

S7. Real-time Monitoring of the DOX Release via Dual-Mode PTI and TPL Imaging in Cancer Cells
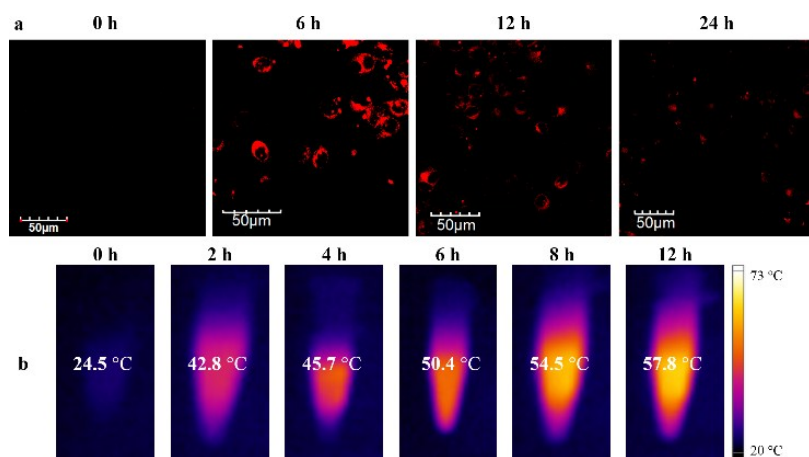

Figure S16. (a) Confocal microscopic images showing the change in the TPL signal intensities in PC-3 cells at different time (cells were incubated with Nanocom-DOX). All images share the same scale bar (50 μm). Images of the cells were obtained using an excitation wavelength of 808 nm, and a long-path (550-650 nm, red signal) emission filter. (b) Temperature images of PC-3 cells suspension under NIR laser irradiation for 5 min, which were recorded by an IR camera at different times (cells were incubated with Nanocom-DOX).
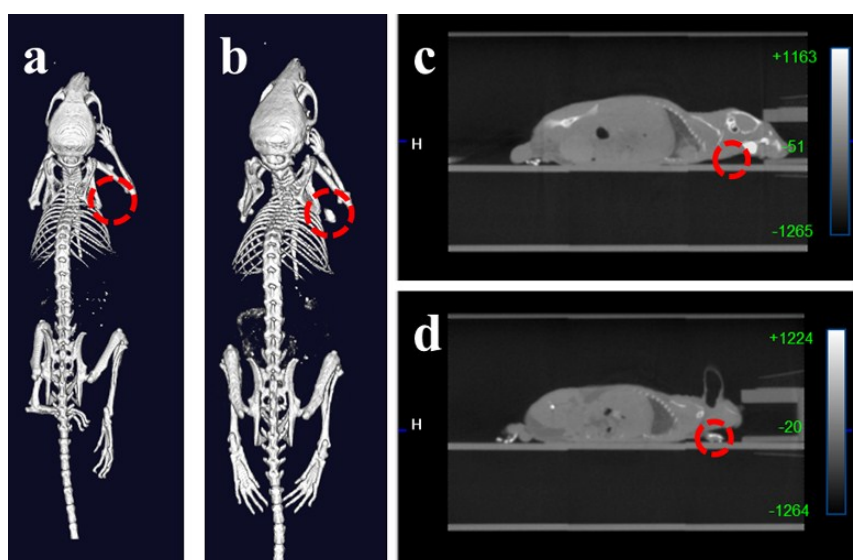
S8. In-vivo X-Ray CT Imaging

Figure S17. CT imaging of a tumor-bearing Balb/c mouse: before (a, c) and after injection with Nanocom-DOX with the dose of 1 mg/kg DOX at 24 h (b, d).

X-ray CT imaging is an important diagnostic imaging technique due to its high resolution and deep tissue penetration. To evaluate the Nanocom-DOX real-time monitoring properties in-vivo, the accumulation of Nanocom-DOX in tumor tissues was evaluated using a murine PC-3 prostate cancer model. Nanocom-DOX was intravenously injected via the tail vein into PC-3 prostate tumor-bearing mice. As shown in Figures S17b,d, the tumor area of the mouse became bright after the injection, thus indicating the accumulation of Nanocom-DOX in the tumor. Nanocom-DOX could be sustained in the tumor for more than 24 h what opens up its application as a possible contrasting agent for CT imaging.

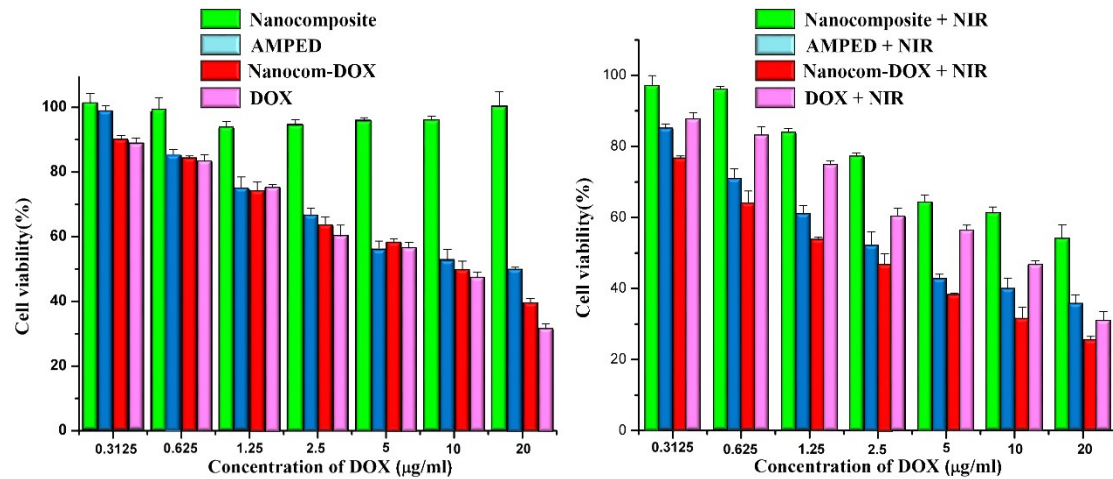## S9. Combined Synergistic Therapy In-vitro and Targeted Delivery

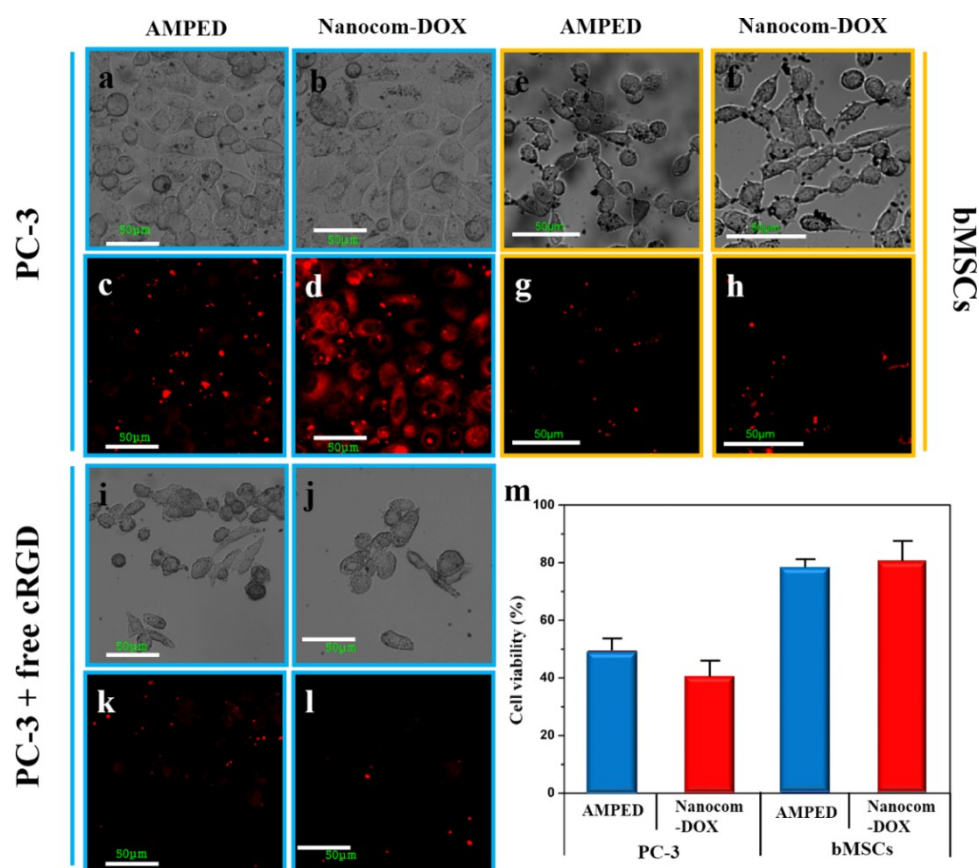**Figure S18.** Cell viability profiles of PC-3 cells.

Figure S19. Cellular uptake of AMPED (without the cRGD ligand) and Nanocom-DOX (with the cRGD ligand) with an AMPE concentration of 25 μg/mL. The incubation time was 3 h (a-l). (a-d) PC-3 cells, (e-h) bMSCs cells, and (i-l) treated with competitive free cRGD peptide. (a), (b), (e), and (f) are the corresponding bright-field images of (c), (d), (g), and (h). Bar = 50 μm. (m) Cytotoxicity of AMPED and Nanocom-DOX incubated with PC-3 cells and bMSCs cells for 12 h.

Table S3. IC_{50} (μg/mL) in PC-3 Cells under different treatments and the calculated CI value.

Free DOX	Nanocom-DOX	Nanocomposite + NIR	Nanocom-DOX + NIR		CI
DOX	DOX	Au-phMSNs	Au-phMSNs	DOX	
4.923	8.585	47.391	11.372	2.274	0.407

To investigate the therapeutic effect of Nanocom-DOX, cell viabilities in different treatments were measured. The quantitative cytotoxicity of the nanocomposite, free DOX and Nanocom-DOX with equivalent doses of DOX was assessed using the MTT assay (Figure S18). For the nanocomposite, cells remain intact even at high concentrations of up to 100 μg/mL. These results are reasonable because all of the four components of the nanocomposite, including the AuNTs, mesoporous silica NPs,

[Eu(THA)$_3$(phen)], and P(NIPAm-co-MAA) polymer brushes, have previously been proven to be of low cytotoxicity and high biocompatibility.[S1,S31-S32] At each concentration, photothermal chemotherapy exhibited the highest cytotoxicity compared with single chemotherapy or photothermal therapy (Figure S18). The IC$_{50}$ data of each treatment are shown in Table S3, and the combination index (CI) was calculated to evaluate the combination effect of different therapies.[S33] In this work, the CI value was 0.407 (<1), which demonstrated the synergistic effect of chemotherapy and photothermal therapy of Nanocom-DOX. Furthermore, the synergistic therapy resulted in a significantly lower IC$_{50}$ for DOX (2.274 μg/mL) compared with that of free DOX (4.923 μg/mL). This finding also implies that Nanocom-DOX can become an efficient cancer cell killing platform.

Furthermore, the targeting ability of Nanocom-DOX was evaluated using the cRGD-unmodified Au-phMSNs@P(NIPAm-co-MAA)@Eu(THA)$_3$(phen)@DOX (named as AMPED) as a control. A measurement of the cellular uptake via confocal microscopy was performed for qualitative evaluation. As shown in Figure S19, Nanocom-DOX exhibited a significantly higher cellular uptake than the unmodified AMPED (Figure S19a-d). Both AMPED and Nanocom-DOX did not show apparent cellular uptake in normal cells (Figure S19e-h). These results demonstrate the targeting ability of cRGD to assist drug delivery systems and to integrate with $\alpha_v\beta_3$-positive cancer cells. Moreover, the addition of a large amount of competing cRGD (Figure S19i-l) significantly inhibited the cellular uptake of Nanocom-DOX in prostatic cancer cell lines (PC-3) (Figure S19d vs. S19l), but it had no apparent impact on that of AMPED (Figure S19c vs. S19k). The cell viability measured via MTT analysis was performed for quantitative evaluation. The higher cytotoxicity somewhat reflects the higher cellular uptake. As shown in Figure S19m, Nanocom-DOX exhibited a significantly higher cytotoxicity in the PC-3 cells, but it had no apparent effect on normal cells compared with AMPED. Because the major distinction of Nanocom-DOX and AMPED is the cRGD modification, the targeting property of cRGD was verified.
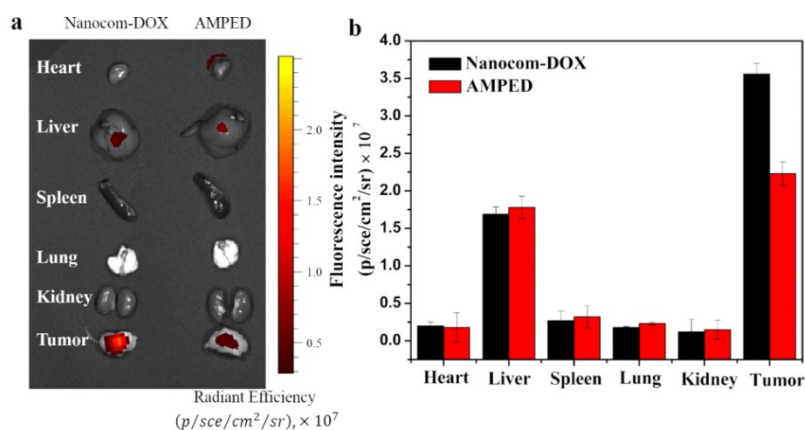
S10. In-vivo Experiments

Figure S20. (a) Ex-vivo fluorescence images of major organs and tumor dissected from mice (implanted with PC-3 cells) after being injected with Nanocom-DOX or AMPED (24 h post injection). These representative images show the greatest fluorescence intensity in the liver and tumor. Taken together, these images suggest clearance of the Nanocom-DOX over time. (b) Semiquantitative biodistribution of Nanocom-DOX or APMED in various organs as determined by the fluorescence intensities measured in (a).

To further investigate the biodistribution of Nanocom-DOX, mice organs were collected 24 h postinjection and imaged ex-vivo. In this experiment, mice were implanted with PC-3 cells, and Nanocom-DOX and AMPED were administered systemically via a tail vein injection after 7 days of tumor growth ($\sim$40 mm^3). After the euthanasia, the organs were explanted and luminescent images were taken with the 808 nm NIR excitation. As shown in Figure S20a, both AMPED and Nanocom-DOX had a superior fluorescence signal in the tumor compared to normal organs. The average fluorescence signal of Nanocom-DOX at the tumor site was 1.6-fold higher than that of AMPED at the tumor site (Figure S20b). A different fluorescence signal between the Nanocom-DOX and AMPED can be explained by the active targeting property of cRGD. There was also accumulation of Nanocom-DOX within the liver, suggesting that Nanocom-DOX might be gradually eliminated by the liver through the bile. Importantly, there was no uptake of Nanocom-DOX in the primary organs associated with the drug and the Eu^{3+} ion toxicity, including the heart, spleen, lung, and kidney, which indicates that Nanocom-DOX has no obvious side effects to these organs.
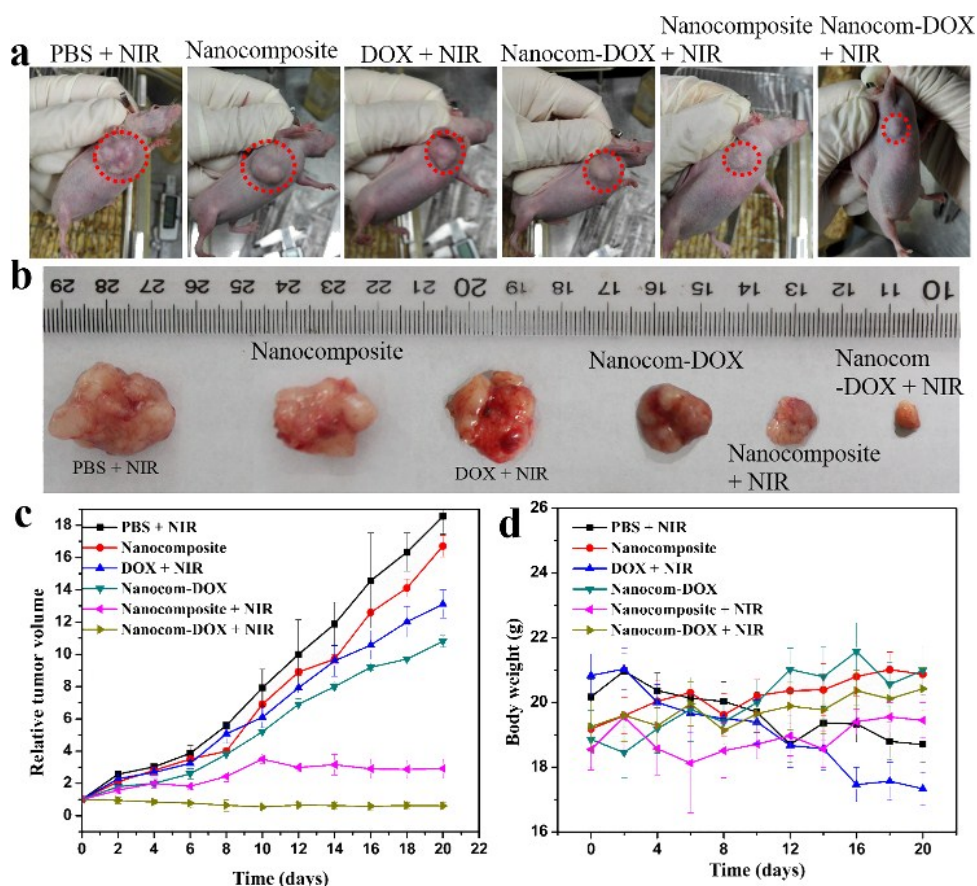
Figure S21. (a) Representative photographs of mice (implanted with PC-3 cells) after various treatments. (b) Photographs of tumor tissue obtained after 20 days. (c) The tumor growth curve. (d) Body weight of PC-3 tumor bearing mice in different groups after treatment.

References of ESI

[S1] Z. J. Hu, X. H. Tian, X. H. Zhao, P. Wang, Q. Zhang, P. P. Sun, J. Y. Wu, J. X. Yang, Y. P. Tian, *Chem. Commun.* 2011, **47**, 12467–12469.

[S2] L. Scarabelli, M. Coronado-Puchau, J. J. Giner-Casares, J. Langer, L. M. Liz-Marzán, *ACS Nano* 2014, **8**, 5833-5842.

[S3] Z. J. Zhang, L. M. Wang, J. Wang, X. M. Jiang, X. H. Li, Z. J. Hu, Y. L. Ji, X. C. Wu, C. Y. Chen, *Adv. Mater.* 2012, **24**, 1418–1423.

[S4] J. Choi, J. Yang, D. Bang, J. Park, J. S. Suh, Y. M. Huh, *Small.* 2012, **8**, 746-753.

[S5] C. M. Lemon, E. Karnas, X. X. Han, O. T. Bruns, T. J. Kempa, D. Fukumura, M. G. Bawendi, R. K. Jain, D. G. Duda, D. G. Nocera, *J. Am. Chem. Soc.* 2015, **137**, 9832−9842.

[S6] C. M. Lemon, E. Karnas, M. G. Bawendi, D. G. Nocera, *Inorg. Chem.* 2013, **52**,

10394−10406.

[S7] J. R. Lakowicz, *Principles of Fluorescence Spectroscopy*, 3rd ed.; Springer: New York, 2006.

[S8] I. Z. Steinberg, *Annu. Rev. Biochem.* 1971, **40**, 83−114.

[S9] F. C. Chen, S. J. Chen, *Opt. Lett.* 2006, **31**, 187−189.

[S10] C. Xu, W.W. Webb, *J. Opt. Soc. Am. B.* 1996, **13**, 481.

[S11] R. Carr, N. H. Evans, D. Parker, *Chem. Soc. Rev.* 2012, **41**, 7673–7686.

[S12] M. C. Heffern, L. M. Matosziuk, T. J. Meade, *Chem. Rev.* 2014, **114**, 4496−4539.

[S13] Y. F. Wang, G. Y. Liu, L. D. Sun, J. W. Xiao, J. C. Zhou, C. H. Yan, *ACS Nano* 2013, **7**, 7200-7206.

[S14] H. Chen, C. Deng, X. Zhang, *Angew. Chem. Int. Ed.* 2010, **49**, 607-611.

[S15] Y. Wang, K. Y. Wang, R. Zhang, X. G. Liu, X. Y. Yan, J. X. Wang, E. Wagner, R. Q. Huang, *ACS Nano* 2014, **8**, 7870–7879.

[S16] Y. Wang, K. Y. Wang, J. F. Zhao, X. G. Liu, J. Bu, X. Y. Yan, R. Q. Huang, *J. Am. Chem. Soc.* 2013, **135**, 4799−4804.

[S17] Z. H. Zhang, C. H. Liu, J. H. Bai, C. C. Wu, Y. Xiao, Y. H. Li, J. Zheng, R. H. Yang, W. H. Tan, *ACS Appl. Mater. Interfaces* 2015, **7**, 6211−6219.

[S18] A. Kumar, S. D. Huo, X. Zhang, J. Liu, A. Tan, S. L. Li, S. B. Jin, X. D. Xue, Y. Y. Zhao, T. J. Ji, L. Han, H. Liu, X. N. Zhang, J. C. Zhang, G. Z. Zou, T. Y. Wang, S. Q. Tang, X. J. Liang, *ACS Nano* 2014, **8**, 4205–4220.

[S19] L. He, Y.;Huang, H. Zhu, G. Pang, W. Zheng, Y. S. Wong, T. Chen, *Adv. Funct. Mater.* 2014*,* **24***,* 2754-2763.

[S20] Zhang, X.; Yang, P.; Dai, Y.; Ma, P.; Li, X.; Cheng, Z.; Hou, Z.; Kang, X.; Li, C.; Lin, J. *Adv. Funct. Mater.* 2013*,* **23***,* 4067-4078.

[S21] C. Tiseanu, V. I. Parvulescu, M. U. Kumke, S. Dobroiu, A. Gessner, S. Simon, *J. Phys. Chem. C.* 2009, **113**, 5784-5791.

[S22] L. R. Melby, N. J. Rose, E. Abramson, J. C. Caris, *J. Am. Chem. Soc.* 1964, **86**, 5117.

[S23] C. Zhang, S. Jin, S. Li, X. Xue, J. Liu, Y. Huang, Y. Jiang, W. Q. Chen, G. Zou, X. J. Liang, *ACS Appl. Mater. Interfaces* 2014, **6**, 5212-5220.

[S24] K. F. Schrum, J. M. Lancaster, S. E. Johnston, S. D. Gilman, *Anal. Chem.* 2000**, 72**, 4317–4321.

[S25] Y. Ma, H. Wang, W. Liu, Q. Wang, J. Xu, Y. Tang, *J. Phys. Chem. B* 2009, **113**, 14139-14145.

[S26] Z. J. Zhang, J. Wang, X. Nie, T. Wen, Y. L. Ji, X. C. Wu, Y. L. Zhao, C. Y. Chen, *J. Am. Chem. Soc.* 2014, **136**, 7317−7326.

[S27] H. Mok, O. Veiseh, C. Fang, F. M. Kievit, F. Y. Wang, J. O. Park, M. Zhang, *Mol. Pharmaceutics* 2010, **7**, 1930-1939.

[S28] S. Padilla-Parra, P. M. Matos, N. Kondo, M. Marin, N. C. Santos, G. B. Melikyan, *Proc. Natl. Acad. Sci. U. S. A.* 2012, **109**, 17627-17632.

[S29] L. M. Pan, J. N. Liu, J. L. Shi, *Adv. Funct. Mater.* 2014, **24**, 7318-7327.

[S30] H. Vihola, A. Laukkanen, L. Valtola, H. Tenhu, J. Hirvonen, *Biomaterials* 2005, **26**, 3055-3064.

[S31] L. Wang, X. Jiang, Y. Ji, R. Bai, Y. Zhao, X. Wu, C. Chen, *Nanoscale* 2013, **5**, 8384-8391.

[S32] T. Asefa, Z. Tao, *Chem. Res. Toxic.* 2012, **25**, 2265-2284.

[S33] S. H. Liu, Y. B. Guo, R. Q. Huang, J. F. Li, S. X. Huang, Y. Y. Kuang, L. Han, C. Jiang, *Biomaterials* 2012, **33**, 4907-4916.